Semiconductor Particle Detectors

University of Manchester, Zhiyu Liu

Novermber 6, 2022

Abstract

Multiple future high-energy physics projects are currently in the planning stages. Future projects require a detector with a high time resolution to distinguish pileup events. This paper provides an overview of semiconductor particle detectors and their ability to provide the required time resolution, beginning with the underlying principles of particle detectors and an example from CMS. SPAD, SiPM, and LGAD are typical semiconductor detectors used in particle physics. Uncertainties in time are caused by the non-uniform energy deposition of incident particles, the inherent electronic noise, and the gain process. The paper concludes with application examples and an outlook for future detectors.

Contents

1 Introduction

Particle detectors have significantly advanced particle physics, leading to the completion of the standard model today. Future projects require detectors with a higher time resolution, a higher radiation tolerance, with compatible size and lower power consumption. Among the various modern detector types, semiconductor detectors offer high time and position resolution and are used in a variety of fields other than particle physics. The incident particles to be detected interact with the detector material in various ways, which is the basic principle of detectors, as shown in section 2. The structure of the semiconductor detector system is depicted in section 3. Detector time resolution is critical in collider experiments, where events pile up significantly, making track reconstruction more difficult, necessitating a time resolution of tens of picoseconds (CMS, [1]). For general semiconductor detectors, this is covered in section 4. A single incident photon can form an effective signal with the internal gain of detectors, significantly increasing detector sensitivity. section 5 goes over this type of avalanche detector. section 6 discusses briefly the practical measurement of time resolution. section 7 and section 8 discuss applications and outlook, respectively.

2 Basic principles

2.1 Interactions of particles with matter

The underlying principle of particle detection is the interactions of particles with matter described by the fundamental forces of the standard model.

2.1.1 *Charged particles interaction with matter*

The electromagnetic force is felt by charged particles. When incident particles interact with the detector, they can interact with either atomic electrons or nuclei. Atomic electrons are excited or ionised as a result of the former. Scintillation can be observed after the excitation. Primary ionised electrons may acquire sufficient energy to ionise nearby electrons, resulting in the formation of a trail of ionisation clusters. During this process, the Bethe formula describes the main energy loss of the incident particles as a function of travelling distance. When incident particles interact with the atomic nuclei, they lose energy in the form of multiple scattering or bremsstrahlung. Since the nucleus is typically much heavier than the particle, repeated scattering due to the Coulomb force results in a negligible loss of energy. Bremsstrahlung is the radiation emitted when the nucleus deflects an incoming particle and is characterised by the radiation length X_0, indicating the distance at which the average energy of the particle beam falls to $1/e$. The types of interactions experienced by incident charged particles depend on their energy. At a few tens of MeV, bremsstrahlung becomes dominant for electrons [2]. Detailed contributions can be found in [3].

Other types of radiation loss are observable under certain conditions. Cherenkov radiation is emitted if the velocity of the charged particle exceeds the speed of light in the material. There is also a possibility of photon emission if a charged particle crosses the boundary between two materials with different dielectric permittivity. This phenomenon is known as transition radiation.

2.1.2 *Photon interactions with matter*

Photon penetration can be described by the Beer-Lambert law as $I = I_0 \exp(-\mu x)$, where μ is the attenuation coefficient depending on the wavelength and the material. The distance X_p represents that the probability has dropped to $1/e$ that a photon has not been absorbed yet, giving an alternative and more frequently used expression $I = I_0 \exp\left(-x/X_p\right)$. Photoelectric effect, Compton scattering, and the production of electron-positron pairs are the possible interactions. In these interactions, photoelectrons, inelastic scattering and two 511 keV annihilation photons can be observed, respectively.

2.1.3 *Neutrino interactions with matter*

Neutrinos can interact with atomic nuclei which are

$$\nu_l + n \rightarrow X + l^- \quad \text{and} \quad \overline{\nu}_l + p \rightarrow X + B^+, \tag{1}$$

where l stands for leptons and X stands for p or n. Leptons in the reaction have a high velocity that exceeds the speed of light in the detector material, so Cherenkov radiation can be detected by photodetectors.

2.2 Detectors overview

In particle physics experiments, we must not only detect the particle's existence, but also acquire additional information about the events. For instance, the kinematics and intrinsic properties of the particles.

In the 19th century, photoemulsion, cloud chamber, and bubble chamber were invented, making it possible to photograph the trajectories of particles. In the 1960s, electronic

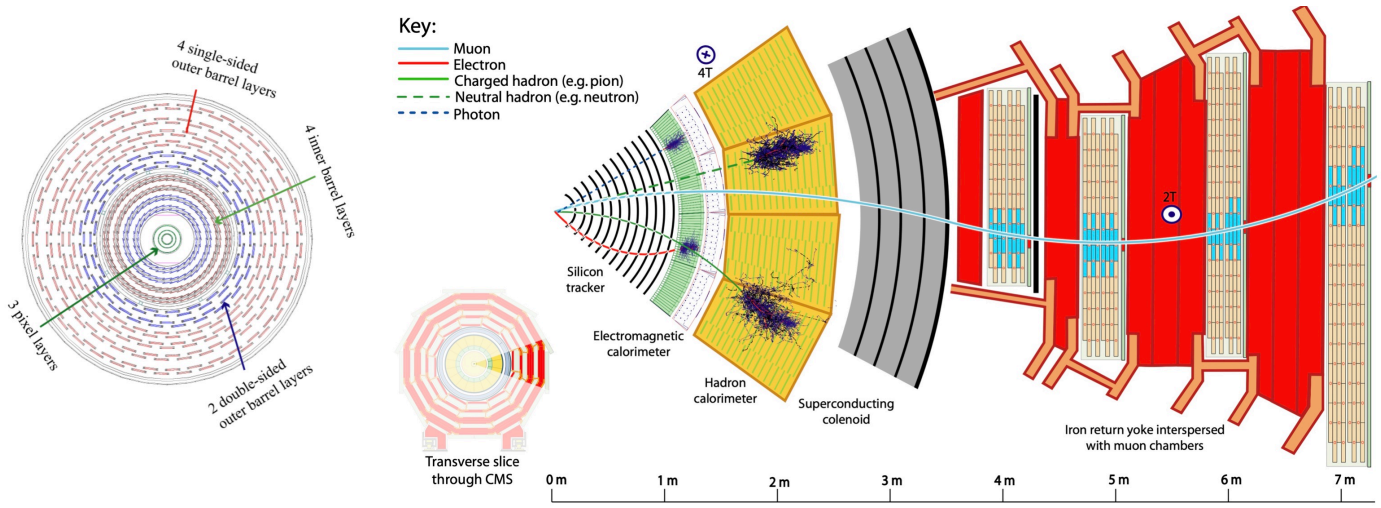

Figure 1: A slice cross section of the CMS (*right*). The innermost layer uses silicon pixel and microstrip detectors to measure the momentum of charged particles. The following electromagnetic calorimeter (ECAL) is constructed from PbWO4, which emits light when electrons and photons pass through and deposit their energy, and on which photodetectors are attached for measuring light. The hadron calorimeter stops hadrons as they pass through the ECAL. The subsequent layer is a superconducting solenoid magnet that generates a magnetic field of 4T. Muons are capable of penetrating all layers, and their momentum are ultimately measured by muon chambers made up of drift tubes, cathode strip chambers, resistive plate chambers, and gas electron multiplier tubes. Interspersed throughout the muon chamber are iron return yokes, which are responsible for the return of magnetic flux and structure support. Details of the silicon tracking system (*left*). The innermost tracking system are composed of three layers of pixel detectors and ten layers of strip detectors. The pixel layers are composed of 124 million $100\,\mu\text{m} \times 150\,\mu\text{m}$ pixels surrounding spherically and two endcap pixel disks at each side. The strip layers consist 15148 modules with strip pitch $83 - 205\,\mu\text{m}$. (images from CMS collaboration)

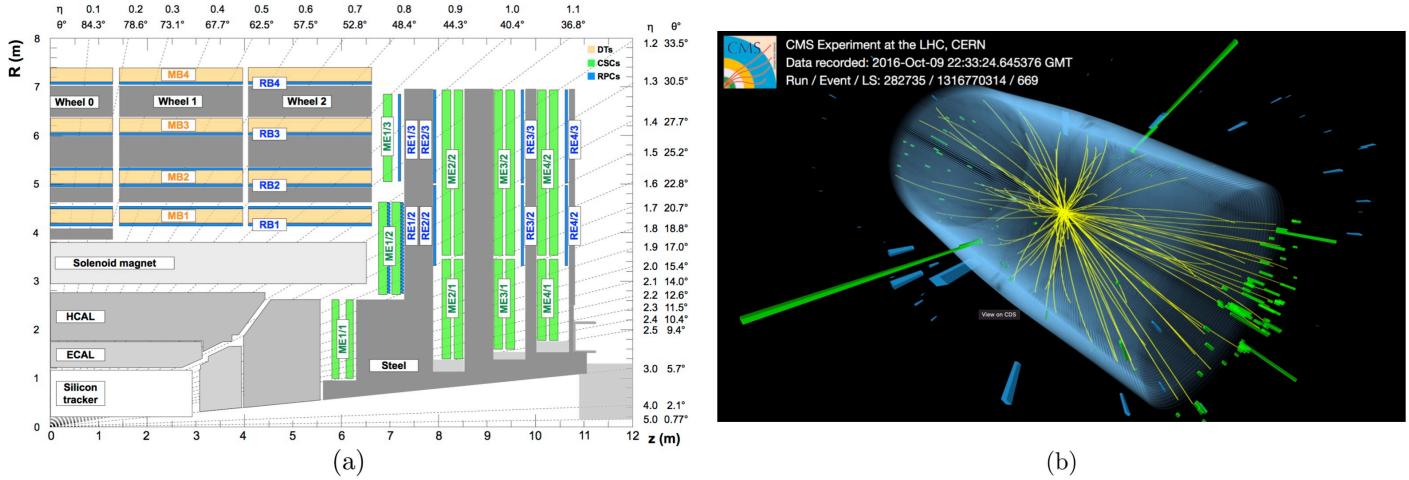

(a) (b)

Figure 2: Quadrant of the CMS detection system and details of the muon detection system [4] (*left*), with pseudorapidity on the axis. The CMS muon detection system is composed of four layers in the barrel (MB) and four planes of endcaps (ME). A reconstructed event showing $H \to \gamma\gamma$, where the energy deposition of photons are demonstrated by the two green towers. (Thomas McCauley/Lucas Taylor/CERN/CMS Collaboration)

recording replaced optical recording as the gas-filled multi-wire proportional chamber (MWPC) was developed. As a result of the advancement of microelectronics, semiconductor detectors have been employed since the 1980s. They typically serve as vertex detectors (The Silicon Vertex Detector at Belle II [5]) and tracking detectors with extraordinary position and time resolution.

Calorimeters are used to measure particle energies in addition to detectors aiming at reconstructing particle tracks. The particles deposit all of their energy within the calorime-

ter, rendering them no longer available for further examination (except neutrinos). Absorption material examples are $PbWO_4$ for CMS Electromagnetic Calorimeter [6], Pb/LAr + Fe for ATLAS Hadronic Calorimeter [7], Ge for gamma ray spectroscopy [8].

The detector system are typically placed in front of the accelerator for fixed-target experiements and spherically surrounded the collider. A slice cross section of the CMS detector system is shown in Figure 1 and Figure 2 as well as an example event.

3 Semiconductor detector systems

3.1 System overview

All semiconductors follow a similar process of timing detection. A sensor absorbs the incoming particles and generates an electronic signal. A preamplifier amplifies and reshapes the signal. The signal is regarded to be effective if it has reached the threshold and time information has been acquired, which referred to as leading edge discrimination. Finally, the time-to-digital converter (TDC) digitises and stores the output signal. The ASIC following the detector may also contain an integrator and an analog-to-digital converter (ADC) for acquiring the energy data.

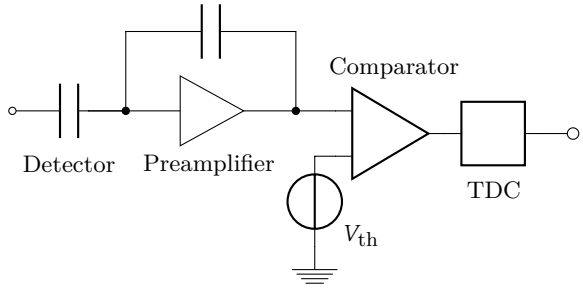

Figure 3: Semiconductor timing detector system. The preamplifier process the raw signal and the comparator determines the effectiveness of the signal and the time information. [a]

[a] This figure was drawn using `circuitikz`, all following figures without sources were drawn by the author of this article.

3.2 Basic detector structures

The semiconductor detectors operate in a manner similar to ionisation chambers. Radiation absorption generates charge pairs that, under the influence of an applied field, move and induce an electrical current in an external circuit, as shown in Figure 4. The $pn-$junction is the fundamental component of semiconductor detectors, and its depletion region serves as the chamber.

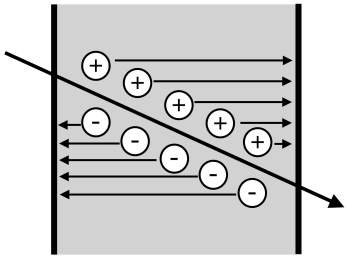

Figure 4: Electrons and holes generated by the radiation move towards respective electrodes and induce a current in the external circiut.

Electrode segmentation, in which electrodes are divided into strips, is a straightforward method for position sensing. But this will cause ghost signals. If two tracks are detected and four strips are activated following orthogonal segmentation of opposite electrodes, there are two sets of possible coordinate as shown in Figure 5 (*left*). This can be resolved by subdividing the electrodes into pixel arrays, whereby both electrodes can provide 2D information as shown in Figure 5 (*right*).

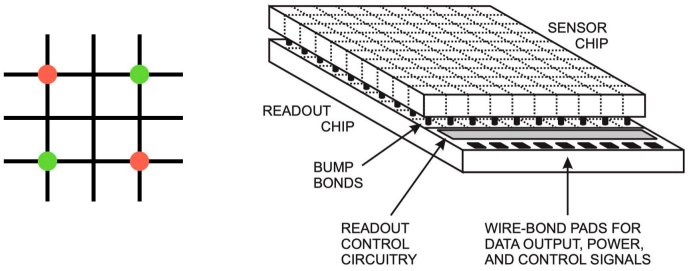

Figure 5: Orthogonal segmentation will generate indistinguishable signals in which the orange and green coordinate pairs cannot be distinguished (*left*). Schematic view of the electrode which can provide 2D position information made up of pixel arrays connected to readout circuits via solder bumps (*right*).

The cross-section of an integrated semiconductor pixel detector reverse-biased diode is shown in Figure 6. Heavily doped $p+$ substrate forms the depletion region at the surface. The guard rings isolate the detection strip by capturing leakage current. The surface is protected by a SiO_2 layer of $100-200$ nm where functional interfaces are connected to outer structures. A bias resistor made of polysilicon (eg: Si_3N_4), a ubiquitous material in silicon electronics, has a resistance of about 2.0 MOhm [9], which is high enough to lower the voltage difference between the strips.

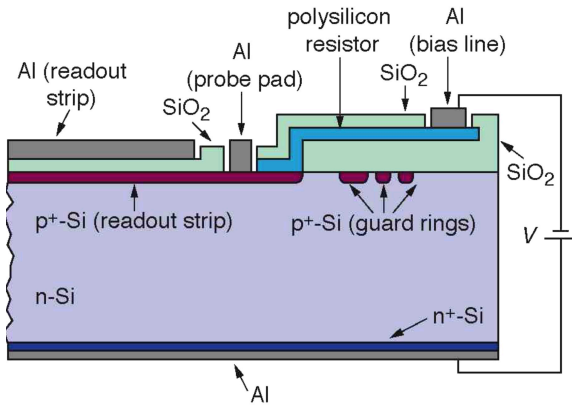

Figure 6: Schematic cross-section of a silicon detector [10].

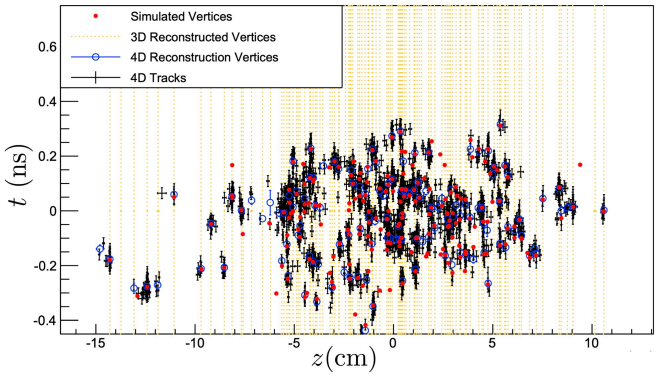

Figure 7: A simulation of vertex reconstruction in a 200 pile-up event. The yellow vertical dashed lines represent 3D reconstructed vertices along which the time information can be used to reconstruct further (Image from [1]).

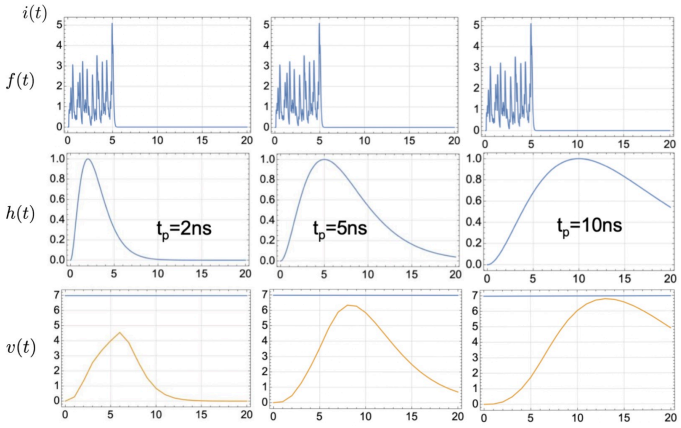

Figure 8: The input signal $f(t)$ being amplified and reshaped by $h(t)$ with different peaking time. When $t_p > T$, the output signal has a pulse-height equal to q. Note that the pulse shapes $f(t)$ here do not represent the signals from the concerning detector, but random signal shapes.

4 Time resolution for general semiconductor detectors

4.1 Time information

Numerous current collision projects focus on rare interactions, including those involving the Higgs boson and dark matter. To increase the likelihood of a successful collision, the number of particles in a bunch is increased. As a result, events pile up and it becomes difficult to distinguish them that occur immediately after. The LHC is experiencing approximately 50 pile-up events with vertices separated by tens of picoseconds. An example of z-vertex distribution in a CMS experiment is shown in Figure 9. However the HL-LHC is expected to deal with a pile-up of 140 vertices. The participance of time information enables 4D tracking in particle reconstruction. We can therefore distinguish different events by their precise occurring time, as shown in Figure 7. In addition to enhancing distinguishability, time information facilitates the reconstruction of events by associating only time-compatible hits.

4.2 Non-uniform energy deposition

The time resolution of a detector depends on a variety of factors. In this section, we discuss the uncertainties that result from non-uniform energy deposition.

4.2.1 *Electronics signal processing*

The charges induced by the $e-h$ pairs is converted to the electronic signal. The signal must be amplified and reshaped in order to provide useful information. Consider an input signal $f(t)$ with a superimposed noise $w(t)$. Depending on the discriminator amplifier device, the processing signal varies. Below is an example of delta response.

$$h(t) = \left(\frac{t}{t_p}\right)^n e^{n(1-t/t_p)}\Theta(t), \tag{2}$$

where $\Theta(t)$ is the Heaviside function and t_p is the peaking time of the signal with $h(t_p) = 1$. The output signal $v(t)$ is the convolution of $f(t)$ and $h(t)$. When the peaking time is longer than the signal duration T, the output signal has an amplitude equal to the total charge of the signal and an approximated displacement t_g which is the centre of gravity time of the signal, as shown in Figure 8.

$$v(t) = \int_0^t h(t-t')f(t')\mathrm{d}t' \approx qh(t-t_g),\ t_g = \frac{1}{q}\int_0^T f(t')\mathrm{d}t' \tag{3}$$

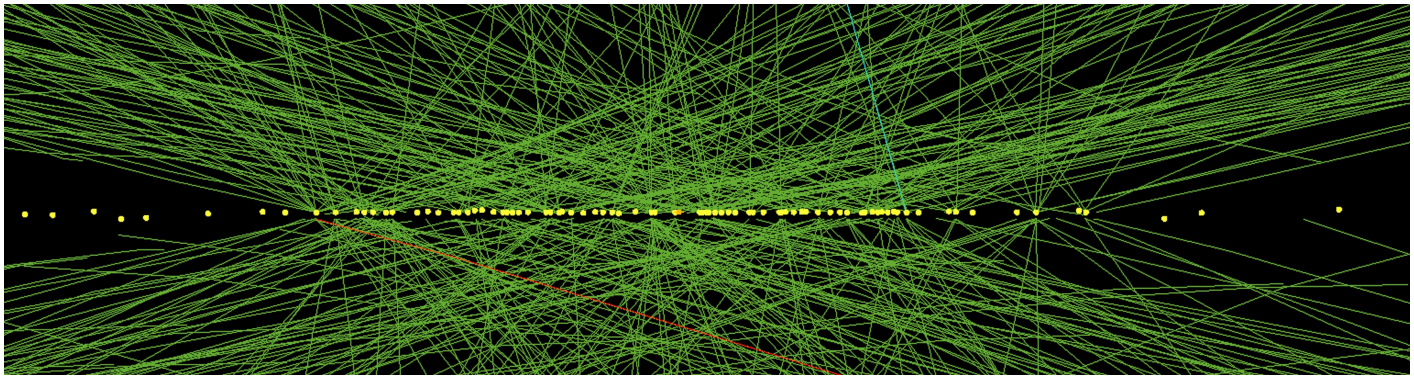

Figure 9: Vertex distribution in the z direction occurring in the same bunch crossing. (CMS-PHO-EVENTS-2012-006-6)

4.2.2 *The time walk effect*

When detecting fast ($\beta\gamma \gtrapprox 3$) and heavy charged particles, in each interaction there is a probability $p_{\text{clu}}(n)$ to produce a cluster of n $e-h$ pairs. If we divide the sensor with thickness d into strips with width Δz, the probability of producing n $e-h$ pairs in Δz is

$$p(n,\Delta z)\mathrm{d}n = \left(1-\frac{\Delta z}{\lambda}\right)\delta(n)\mathrm{d}n + \frac{\Delta z}{\lambda}p_{\text{clu}}(n)\mathrm{d}n, \tag{4}$$

where $\lambda \approx 0.21\,\mu$m is the average distance between interactions in silicon [11] and we assume only one event will take place in Δz. The probability of having n $e-h$ pairs in the sensor can be calculated via the convolution theorem.

$$P(s,d) = \mathcal{L}[p(n,d)] = \mathcal{L}[p(n,\Delta z)]^N = \left[1+\frac{d}{\lambda N}(P_{\text{clu}}(s)-1)\right]^N,$$
$$p(n,d) = \mathcal{L}^{-1}\left[e^{d/\lambda(P_{\text{clu}}(s)-1)}\right]. \tag{5}$$

Since the $e-h$ pairs created in each measurement obey a distribution described by (5), the amplitude and shape of the signal varies in each measurement, with simulations shown in Figure 10, where the total currents were 2.5 μA and 1.6 μA for the two runs. This would cause a time walk uncertainty due to different time of reaching the threshold. If we use Landau's approximation of $p_{\text{clu}}(s)$, the uncertainty is called the Landau fluctuation. This is shown in Figure 11 (a).

The Landau fluctuation is determined by the r.m.s. value of t_g. The result is given by

$$\Delta t_g = w(d)\sqrt{\frac{4}{180}\frac{d^2}{v_e^2} - \frac{7}{180}\frac{d^2}{v_e v_h} + \frac{4}{180}\frac{d^2}{v_h^2}}, \tag{6}$$

$$w^2(d) = \frac{1}{\ln(d/\lambda)} \quad \text{(Landau)}, \tag{7}$$

where v_e, v_h are drift velocities of electrons and holes, respectively. If we set $v_e = v_h$, Equation 6 reduces to

$$\Delta t_g = w(d)\frac{1}{\sqrt{180}}\frac{d}{v} \approx 0.075 w(d) T. \tag{8}$$

For a 50 μm sensor, $\Delta t_g \approx 0.075 \times 0.2 \times 650$ ps $= 10$ ps.

From Equation 6 and Equation 7 we can see that a thinner sensor yields less Landau fluctuations. The theoretical

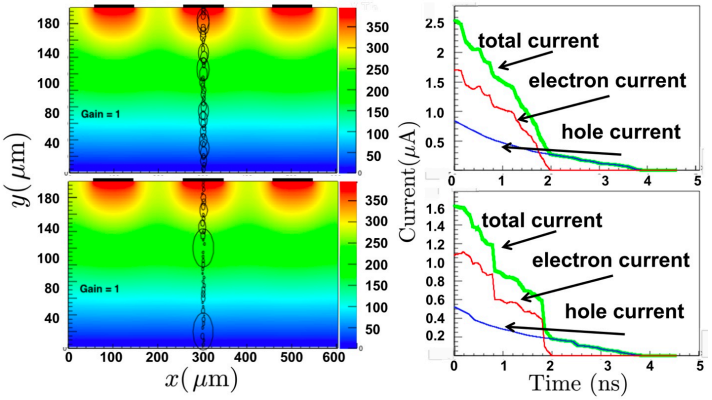

Figure 10: Simulations of energy deposit using *Weightfield2*. The left figure is the visualisation of the weight field for a pixellated detector, with clusters representing the energy deposition. The right figure shows the current signal for electrons and holes [12].

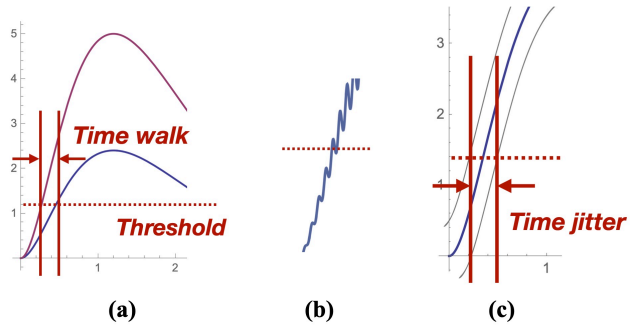

Figure 11: Factors of time resolution. (a) The time walk uncertainty caused by Landau fluctuations. (b) The effect of noise shown schematically. (c) The time jitter resulted from the noise.

time resolution of both Landau and PAI model (another model for $p_{\text{clu}}(s)$) are shown below. Theoretically, a 50-micron sensor's intrinsic time resolution can reach 10 picoseconds.

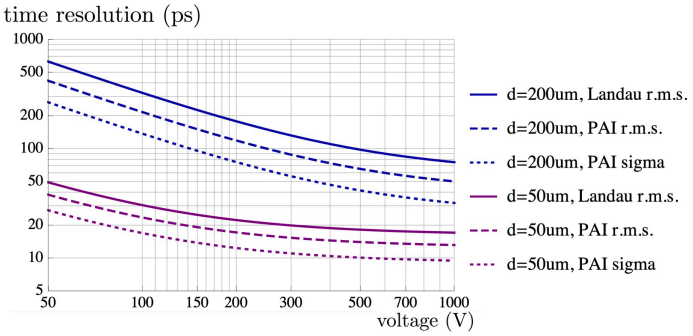

Figure 12: Time resolution due to non-uniform energy deposition as a function of bias voltage for different thickness. [13]

4.2.3 *Mitigation of time walk effect*

Besides the varying energy deposition of incident particles, the signal shape can be affected by the imperfection preamplifier. Experiments with contemporary devices indicate that the amplitude of the impulse response function provided by the preamplifier has an uncertainty of 20 to 30 mV (Gaussian r.m.s.). Also observed is that the preamplifier becomes non-linear at amplitudes greater than 800 mV, meaning that the magnification factors are different for different signal amplitudes [14].

Fortunately, the time walk effect can be significantly reduced by existing algorithms [15]. The Time-over-Threshold (ToT) method adjusts the arrival time by measuring the time interval of detected signals that exceed the threshold [16]. Instead of a fixed value, the Constant Fraction Discriminator (CDF) technique uses a fraction of the amplitude as the threshold. The optimal fraction can be determined through preliminary tests.

4.2.4 *Drift velocity of electrons and holes*

Maintaining a constant drift velocity is essential for achieving a high time resolution, as seen from the discussion above. The drift velocity of electrons and holes saturate at around $10^7 \text{cm/s} = 0.1\,\mu\text{m/ps}$ at high fields as shown in Figure 13, such that it takes 1000 ps for an electron to travel through a detector that is 100 microns thick. It is evident that by decreasing the temperature, the saturation velocity can be attained at lower fields.

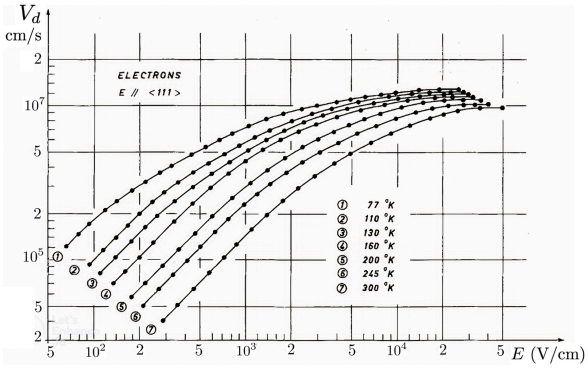

Figure 13: Drift velocity of electrons at different temperatures. [17]

4.3 Noise

The signal is always superimposed with a background noise, which can lead to uncertainties when compared to the threshold as shown in Figure 11 (b). This noise can be quantified through the slope of the signal, the resulting uncertainty is called the time jitter, as shown in Figure 11 (c). The signal-to-noise ratio (SNR) is essential for the amplitude measurement, while the slope-to-noise ratio manifest the time resolution, both being critical in the signal analysis. Using simple geometry, one can show that the time jitter is inversely proportional to the slew rate (signal slope). So a fast rise time indicates better resolution, which can be achieved by making the sensor thinner.

Consider a signal $f(t)$ with superimposed noise $w(t)$ being processed by a filter transfer function $h(t)$. The resulting signal $g(t)$ and the amplitude of noise σ are given by

$$g(t) = \frac{1}{2\pi}\int_{-\infty}^{\infty} F(\mathrm{i}\omega)H(\mathrm{i}\omega)e^{\mathrm{i}\omega t}\mathrm{d}\omega, \tag{9}$$

$$\sigma^2 = \frac{1}{2\pi}\int_{0}^{\infty} W(\mathrm{i}\omega)|H(\mathrm{i}\omega)|^2\mathrm{d}\omega. \tag{10}$$

The formulas can help us find the optimal SNR $\frac{g(t)}{\sigma}$ and slope-to-noise ratio $\frac{g'(t)}{\sigma}$. It is shown that they both reach their maximum value for the optimal transfer function [13]. While the theoretical optimum cannot be attained in practise, we typically use a transfer function $h(t)$ in the form as Equation 2, where we have to determine the peaking time t_p to gain the optimal SNR and slew rate. The best peaking time is around $1-1.5\ T$ with T being the signal duration. Combining the intrinsic time uncertainty and the amplifier noise, we have a time resolution

$$\sigma = \sigma_{\text{Landau}} \oplus \sigma_{\text{jitter}} = \sqrt{\sigma^2_{\text{Landau}} + \sigma^2_{\text{jitter}}} \tag{11}$$

4.4 Signal distortion

Coupling time information with position resolution generates an additional source of uncertainty. In contrast to parallel plate chambers, pixelated detectors distort the electric field. So the pixel size and pitch distance should be taken into consideration.

4.4.1 *The Shockley-Ramo theorem*

When ionised electrons move towards electrodes, induced charges generate a current and thus an electronic signal. Previously when doing theoretical signal analysis, one need to integrate the time-varying charges on the electrodes. The Schockley-Ramo theorem states that the current induced by the electrons is given by

$$i(t) = -q\boldsymbol{v}\cdot\mathbf{E}_W, \tag{12}$$

where $\boldsymbol{v}$ is the electron drift velocity and $\mathbf{E}_W$ is the weighting field. The weighting field is computed when the potential of the selected electrode is unit, all others are zero and charges having been removed. As a result of the weighting field being dependent solely on the geometric shape of the sensor, the theoretical signal can be evaluated conveniently.

4.4.2 *Weighting field fluctuations*

The discussion above indicates that the signal is highly influenced by the geometry of the sensor. Figure 14 compares the weighting field for wide and narrow pixels, consequently the trajectory of the electrons and holes will be different and the signal will be distorted from the simplest parallel-plate sensor.

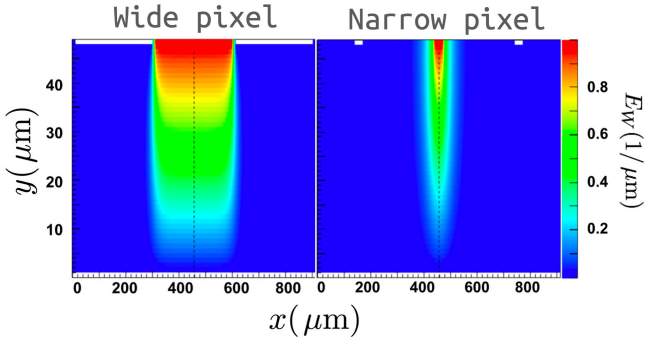

Figure 14: Weighting field simulation for wide and narrow configuration of pixel detectors [12].

Consider a sensor placed from $z = 0$ to $z = d$ and pairs of charges constitute a uniform line between the sensor plates as shown in Figure 15 and the current is given as

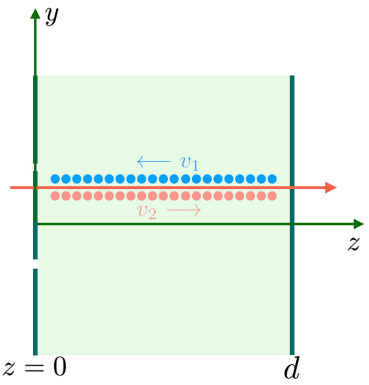

Figure 15: Charge pairs forming a uniform line and travelling towards corresponding electrodes in the sensor, as seen in a schematic. The electrons are shown in blue with drift velocity v_1, and their electrode is pixelated.

$$\frac{I(x,y,t)}{q_{\text{line}}} = -v_1\int_0^d E_w[x,y,z-v_1t]\Theta[z/v_1-t]dz - v_2\int_0^d E_w[x,y,z+v_2t]\Theta[(d-z)/v_2-t]dz \tag{13}$$

The time resolution is evaluated by calculating the standard deviation of the centroid time $\tau = \int i(t)t\mathrm{d}t/\int i(t)\mathrm{d}t$. Substituting Equation 13 yields

$$\sigma^2_{\text{Distortion}} = \tau^2_{\text{rms}} = d^2\left(\frac{c_{11}}{v_1^2}+\frac{c_{12}}{v_1v_2}+\frac{c_{22}}{v_2^2}\right), \tag{14}$$

where c_{11}, c_{12}, c_{22} are constants depending on the pixel size w (geometry) and sensor width d. Furthermore, the Landau fluctuations and the weighting field fluctuations have a high correlation at certain values of w/d. By taking this into consideration the complete result is given by

$$\sigma = w^2(d)\left(\frac{k_{11}d^2}{v_1^2}+\frac{k_{12}d^2}{v_1v_2}+\frac{k_{22}d^2}{v_2^2}\right)+\left(\frac{c_{11}d^2}{v_1^2}+\frac{c_{12}d^2}{v_1v_2}+\frac{c_{22}d^2}{v_2^2}\right), \tag{15}$$

where k_{11}, k_{12}, k_{22} are again constants depending on w/d. When $w/d \gg 1$, we have $k_{11} = k_{22} = \frac{4}{180}, k_{12} = -\frac{7}{180}$, in coordination with Equation 6. The numerical results of time resolution is shown in Figure 16. This section is based on [13], where detailed evaluations can be found.

4.5 TDC uncertainties

The TDC outputs the time difference between the set start and stop point of each pulse. Basic TDC contains a clock with period ΔT and the time is given by counting the cycles. This device gives an inherent time uncertainty of $\Delta T/\sqrt{12}$ on the order of few ps.

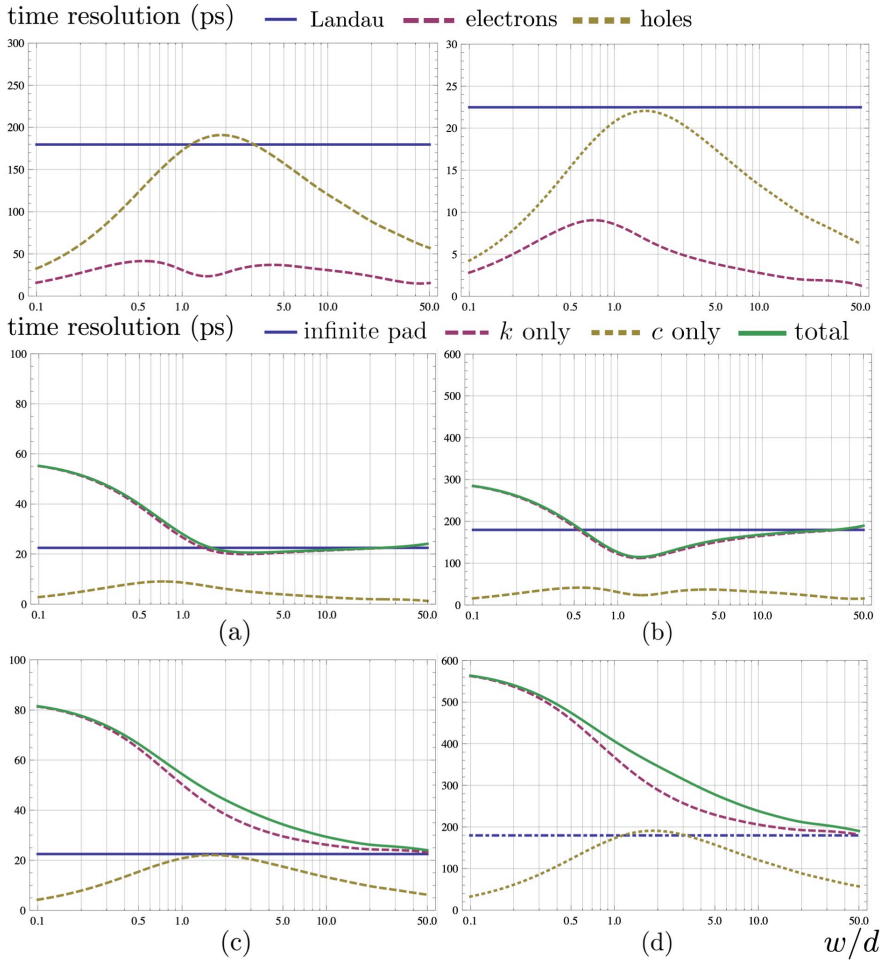

Figure 16: Numerical results of time resolution for semiconductor detectors. The x-axis is the geometric property w/d of the sensor. In the above two figures, the horizontal line represent the resolution for sensors with thickness $d = 200\,\mu$m *(left)* and $d = 50\,\mu$m *(right)* due to Landau fluctuations only. The curves represent the weighting field fluctuation for electrons and holes. A maximum value can be found around $w/d = 1$.
The below four figures are numerical results from Equation 15 for sensors with thickness $d = 200\,\mu$m $(a)(c)$ or $d = 50\,\mu$m $(b)(d)$ and for electrons $(a)(b)$ or holes $(c)(d)$ being the carriers moving towards the pixel. For small pixel sizes, the Landau fluctuations correlate strongly with the weighting field fluctuations. The total resolution for the thinner sensor can reach 20 ps for an optimal w/d. [13]

5 Avalanche-based detectors

5.1 Overview

5.1.1 *APD and SPAD*

The gain is critical when detecting low energy radiations, such as X-rays from less active radioactive sources. If the electric field in the detector's active area is strong enough, an avalanche will occur, resulting in the detector's internal gain. This can be achieved by doping and applying a high reverse biased voltage. The $I-V$ characteristic curve of the pn–junction is shown in Figure 17. The detector working in the linear mode is typically called linear mode avalanche photodiode (LM-APD). The gain is predictable and shows uniformity in the active region [18]. The single photon avalanche diode (SPAD) works in the Geiger mode, where a single photon entering the detector can lead to an avalanche.

The cross section of the SPAD is shown in Figure 18. Since the absorption length of photons in silicon will exceed 1 μm, to fully absorb broadband photons a conversion layer of $10-100\,\mu$m is frequently needed [19]. The electrons created in the conversion layer drift to the gain layer and trigger the avalanche. As for charged particles the mean free path $\lambda \approx 0.21\,\mu$m thus the conversion layer is not essential.

Inside the gain layer, the probability of an electron (hole) to create an $e-h$ pair is given by $\alpha(x)\mathrm{d}x$ $(\beta(x)\mathrm{d}x)$, where α, β are impact ionisation coefficients growing with the field strength and $1/\alpha$ $(1/\beta)$ are the average travel distances before an electron (hole) creates an $e-h$ pair. The theoretical breakdown condition is given by

$$d_g > \frac{1}{\alpha-\beta}\ln\left(\frac{\alpha}{\beta}\right), \tag{16}$$

where d_g is the gain layer thickness.

During the avalanche, electrons and holes congregate at the electrodes, forming an electric field opposite the biassed voltage. Unless the voltage is reduced and the diode returns to its previous state, the diode will remain in this state with a reverse current flowing through it. This can be resolved by connecting an in-series resistor that will have an increasing

voltage drop during the avalanche, as shown in Figure 17. With a recharge time constant on the order of 100 ns at room temperature [20], this dead-time and recharging process restrict the SPAD from concurrently detecting photons.

5.1.2 *SiPM*

The silicon photomultiplier (SiPM) incorporates a 2D array of SPAD detectors, each of which can detect a single photon. It is also called the multi-pixel photon counter (MPPC). If the SPADs are coupled with a common TDC, the device is known as a digital silicon photomultiplier (dSiPM) [21, 22], and its arrival timestamp is determined by the first photon detected. If each SPAD is coupled to a TDC, they are referred to as SPAD-TDC arrays [23]. The size of SiPM is typically on the order of $1\,\mathrm{mm}^2$, with SPADs on the order of several microns.

Compared to traditional photomultiplier detectors (PMT), the silicon photomultipliers have immunity to the magnetic field, a low operating voltage, compactness, higher radiopurity, ruggedness and large scale fabrication possibilities [24].

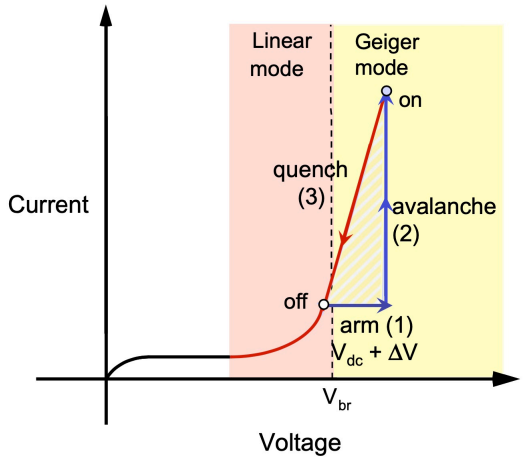

Figure 17: $I-V$ characteristic curve for reverse biased pn–junction as well as the quenching effect [25].

5.1.3 *LGAD and UFSD*

The internal gain of avalanche-based semiconductors such as APD and SPAD enables the detection of a single incident photon. However, high gain increases sensor noise and makes segmentation difficult due to high fields. The optimal gain for the best resolution is not high enough for single photon detecting. The low gain avalanche detector (LGAD) are intended for the detection of charged particles with greater energy, so a low gain is permissible. LGAD adds a p–type layer with moderate doping beneath the n–type layer with high doping. This increases the strength of the electric field, meeting the conditions for avalanche without the help of high excess bias voltage, as shown in Figure 18 (b) together with the pulse shape (c).

Considerations about better space-time resolution to deal with pile-up events and capability of withstand radiation damage ($> 1\times10^{17}\ n_{eq}/\mathrm{cm}^2$), the development of the ultra fast silicon detector (UFSD) is progressing under the charge of CERN RD50 collaboration [27]. The UFSD is expected to be the component of the High Granularity Timing Detector (HGTD) for the HL-LHC [28] and CMS-TOTEM Precision Proton Spectrometer (CT-PPS) [29] , aiming at 10 ps resolution.

5.2 Time resolution of avalanche-based detectors

5.2.1 *Fluctuations in the conversion layer*

In the case of photon detection, the arrival time of electrons drifting to the gain layer is dependent on the absorption position in the conversion layer, which is a distribution determined by the absorption length of photons X_p and the the conversion layer thickness d_c. This gives rise to the **arrival time uncertainty**. The probability for a single photon to be absorbed in $[x_0, x_0+\mathrm{d}x_0]$ is given by $P^*(x_0)\mathrm{d}x_0 = 1/X_p e^{-x_0/X_p}\mathrm{d}x_0$. Since we only concern the effective photons, the probability needs to be normalized by the cumulant probability of being absorbed in the conversion layer $p = 1-e^{-d_c/X_p}$, yielding

$$P(x_0)\mathrm{d}x_0 = \frac{1}{1-e^{d_c/X_p}}\frac{1}{X_p}e^{-x_0/X_p}\Theta(d_c-x_0)\mathrm{d}x_0. \tag{17}$$

The arrival time distribution is thus

$$\rho(t) = \int_0^{d_c} P(x_0)\delta\left[t-\frac{d_c-x_0}{v_e}\right]\mathrm{d}x_0, \tag{18}$$

from which we can calculate the uncertainty of the arrival time and the result is given by [19]:

$$\sigma^2_{\mathrm{arrival}} = \int_0^T t^2\rho_1((t)\mathrm{d}t - \left(\int_0^T t\rho_1(t)\mathrm{d}t\right) \tag{19}$$

$$= T^2\left[\frac{X_p^2}{d_c^2} - 4\sinh^{-1}\left(\frac{d_c}{2X_p}\right)^2\right]. \tag{20}$$

Apart from the contribution of varying interaction positions, the diffusion also has an impact on the time resolution. For an electron at $(x_0, t=0)$, the probability $p(x, x_0, t)$ of finding the electron at (x,t) is a Gaussian distribution with standard deviation $\sigma_D(t) = \sqrt{2Dt}$, where D is the diffusion coefficient. The additional arrival time resolution term

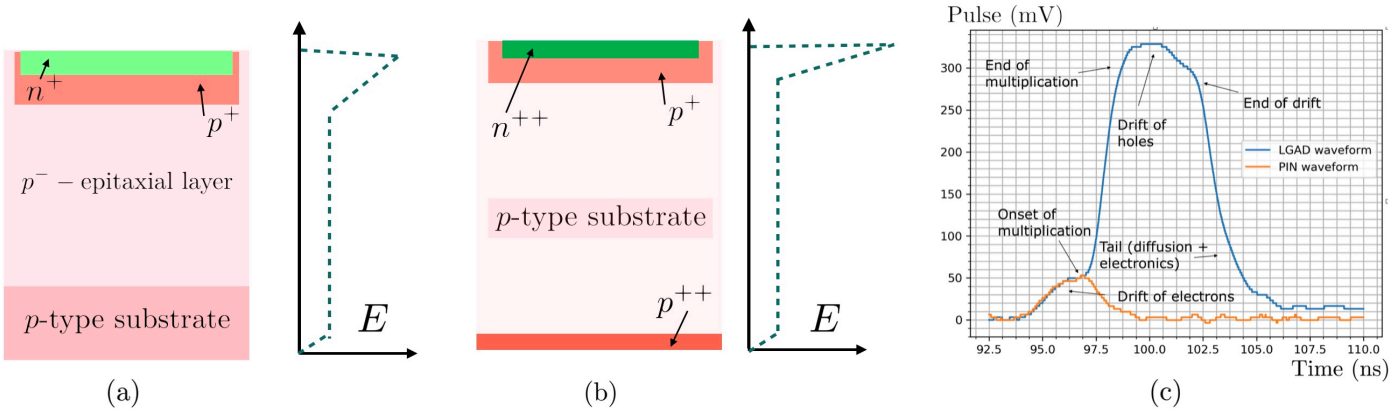

Figure 18: Schematic cross sections of the SPAD (a) and LGAD (b) with the qualitative strength of their electric fields (a). The pulse shape of the LGAD (c) [26]

due to diffusion is given by

$$\sigma^2_{\text{Diffusion}} = \frac{2DT}{v_e^2}\left(\frac{1}{1-e^{-d_c/X_p}} - \frac{X_p}{d_c}\right) + \frac{8D^2}{v_e^4}. \tag{21}$$

The numerical result of time resolution due to arrival time in limiting conditions is shown in Table 1. If $X_p \gg d_c$ the absorbing position is considered to be uniform across the conversion layer.

Table 1: Time resolution as a result of the varying time spent in the conversion layer. The drift velocity is assumed saturated and $D = 35\text{cm}^2/\text{s}$.

Condition	d_c (μm)	σ_{Arrival} (ps)
$X_p \gg d_c$	1/10/100 μm	2.89/28.9/289
$X_p \ll d_c$	1/10/100 μm	1.6/8.37/26.46

5.2.2 *Fluctuations in the gain layer*

Since the signal amplitude is proportional to the amount of charge produced. A threshold of the number of charge can be set to determine the time resolution. The avalanche fluctuations yield different amount of $e-h$ pairs, which result in the threshold crossing time uncertainty. This is described by the time response function $\rho(n,t)\mathrm{d}t$ representing the signal has reached the n-pairs threshold. The time resolution is calculated in the same way as Equation 19. The results demonstrate that the avalanche uncertainty is independent of the threshold, as the number of generated electrons and holes fluctuates initially and then increases exponentially by a constant factor, as seen in Figure 19. The result is given by

$$(\gamma v^*)^2 \sigma^2_{\text{ava}} = \frac{\pi^2}{6}, \tag{22}$$

where $v^* = 2v_e v_h/(v_e + v_h) \approx 0.1\ \mu\text{m/ps}$ in saturation and γ is dependent on the electric field and gain layer thickness.

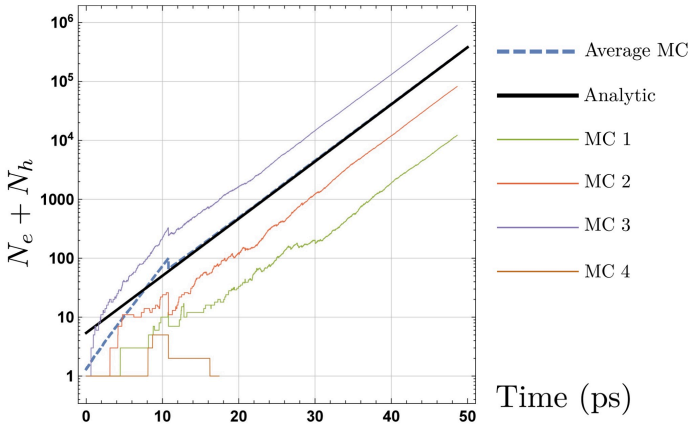

Figure 19: Monte Carlo simulations and analytic results for an $e-h$ avalanche starting from a single electron. After the initial fluctuations the avalanche grows exponentially with a stable factor. The MC4 shows an avalanche breakdown scenario [19].

In addition, for detectors without a conversion layer and photons that have not been absorbed by the conversion layer, the varying interaction position of photons contributes to the overall uncertainty as well. An approximated result of the combined time resolution is given by

$$\sigma_{\text{gain}} \approx \frac{c_0}{\gamma v^*}, \tag{23}$$

where $c_0 \approx 1-3$. Numerical results are demonstrated in Figure 20 (a) for varying gain layer thickness. The contributions from avalanche fluctuations and varying position are shown in Figure 20 (b).

5.2.3 *Time resolution when detecting charged particles*

In the case of charged particles, the conversion layer is no longer needed. The incident particles will leave a trail of clusters in the gain layer, as seen in subsubsection 4.2.2. Therefore, the growth of avalanche will be affected by the number of $e-h$ pairs in the primary cluster. The numerical results of the time resolution are given by $(0.8-2.5)/\gamma v^*$, as shown in Figure 20 (c).

5.2.4 *Noise*

The predominant sources of background noise are the dark count rate (DCR) and afterpulsing. Other effects reported include the twilight effect [31] and charge persistence [32]. This type of statistical noise is distinct from the intrinsic electronic noise that is superimposed on the signal pulse, as discussed in subsection 4.3.

The thermal fluctuation of carriers will generate electrons and holes without any photons entering the detector, which is called the dark current. The DCR is measured in terms of effective counts in a unit of time without sources. The rate increases with increasing temperature bias voltage. According to research, the primary source of DCR is the energy levels within the bandgap caused by impurities in the material [33]. Tests have demonstrated that SiPM has a DCR on the order of 1×10^5 cps/mm^2 at room temperature and 6 V of excess bias voltage ($V-V_{\mathrm{br}}$) [34, 35, 36]. At cryogenic temperature (below 100 K) The DCR can go as low to 0.01 cps/mm^2 for SiPMs developed at FBK [20].

During the avalanche, the carriers at the conduction band can fall into deep and shallow traps within the bandgap and trigger a secondary avalanche when released, which is called the afterpulse.

5.2.5 *Time resolution of SiPM*

The time resolution of SiPM is determined by the superposition of its constituent SPADs. Therefore, uniformity between cells is essential. However, for large pad SiPMs, the cells' varying trace impedances can result in significant timing resolution differences between cells [37].

5.2.6 *Time resolution of LGAD*

The effect of geometric properties on the time resolution of LGAD has been directly investigated through experiments. The pulse shape scales as the thickness of LGAD increases, due to the multiplied holes travelling backwards. For instance, the collection time of 1 ns for 50 μm LGAD becomes 9 ns for 300 μm thickness [38]. The thickness has no effect on the amplitude of the output signal for a fixed gain, whereas the rise time is approximately inversely proportional to the thickness. The combined effect of gain and thickness on the slew rate is given by $\mathrm{d}V/\mathrm{d}t \propto G/d$ [39].

5.2.7 *Summary of time uncertainty sources*

For general semiconductor detectors, such as no-gain PIN and avalanche-based APD, the contributions of time resolution are as follows: (i) The time walk effect, which is caused by the non-uniform energy deposition of charged incident particles (Landau fluctuations) and the imperfection of amplifier devices. Multiple algorithms can mitigate this issue. (ii) The time jitter is caused by the intrinsic electronic noise and background noise superimposed on the signal. This is determined based on the slope-to-noise ratio. The faster rise time is attained by thinning the sensor and applying a stronger field. (iii) The weight field distortion in pixel detectors. This is the result of simultaneously satisfying the position resolution and time resolution. The optimal strip-pitch ratio is determined jointly by less weight field influence and precise position resolution. (iv) The inherent resolution of the TDC, which is constrained by its clock period.

For avalanche-based semiconductor detectors, the following additional contributions must be considered. (v) The varying arrival time to the gain layer in detectors with a conversion layer, as a result of absorption position and diffusion, which is determined by the layer thickness and field strength. (vi) The avalanche fluctuations in the gain layer, which correlate the Landau fluctuations during the detection of charged particles. (vii) For SiPM, the overall resolution is determined by cell-to-cell uniformity.

5.2.8 *Limitations on the time resolution*

The ultimate limit on the time resolution is the non-uniform energy deposition of incident particles. The theoretical limit time resolution can reach to $1-3$ ps as seen in Figure 20. The electronic intrinsic noise also sets the limit to the final resolution. The most recent report have demonstrated a TDC with 4.8 ps resolution [40]. In fact the progress of SiPM products have been more productive than front-end readout electronics these years.

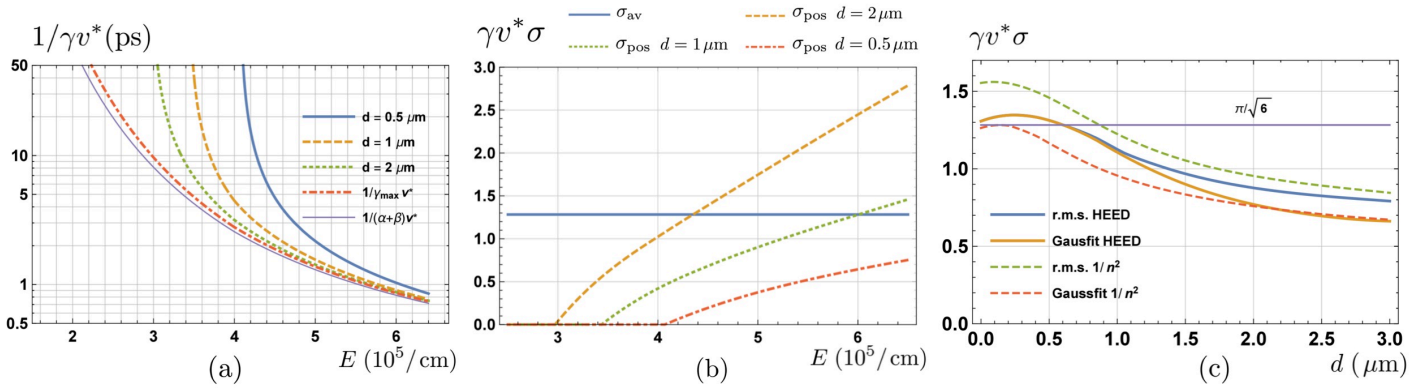

Figure 20: (a) Time resolution factor $1/\gamma v^*$ for different gain layer thickness as a function of field strength. (b) Contributions of avalanche fluctuations and the varying position. The avalanche fluctuations contribution is constant as seen from Equation 22. (c) Time resolution for charged particles as a function of gain layer thickness. The solid lines employ the Landau distribution, while the dashed lines assume the deposition follows a $1/n^2$ probability. HEED stands for the calculation program [30]. (Images all from [19])

6 Measurements of time resolution

Regardless of the incident particle type, the methods for measuring detector time resolution are all statistical methods. Experiments employ more than two detectors that are thought to be identical. They are stacked with some distance between them, allowing incident particles to be detected successively. The difference or average of detection time is then investigated, which is typically Gaussian. The FWHM of the distribution is regarded as the resolution. Assume the time resolution for two detectors are σ_1 and σ_2, then the time difference has a resolution of $\sigma = \sqrt{\sigma_1^2 + \sigma_2^2} \overset{\sigma_1=\sigma_2}{=\!=\!=} \sqrt{2}\sigma_1$. When using a laser as the test source, only time jitter contributes, whereas Landau fluctuation must also be considered when using particle beams. Examples of experiment setup and test results are shown in Figure 21 and Figure 22. Recent beam tests on UFSD have reached 16 ps resolution for a 230 V bias voltage [14].

7 Applications

The choice of photodetectors depend on the detection type, detector size compared to the available space, working environment as well as the price. For instance in large scale particle physics APDs are often used due to price and space. A thorough review of applications can be found in [57]. In the following some specific applications are introduced and selected applications are shown in Table 2.

In diffuse optics, photons travel through highly scattering media, such as biological tissues, carrying information about how the medium absorbs and scatters light. For instance, haemoglobin and deoxygenated-haemoglobin absorb specific wavelength ranges, and the scattered photons can be used to determine the haemoglobin concentration [45]. Photodetectors also have potential applications in oximetry of and mammography [58, 59].

Weakly interacting massive particles (WIMP) are hypothetical dark matter candidates. WIMP particles interact with target nuclei by either a recoiling mechanism resulting in de-excitation scintillation or the formation of excimers, both of which provide an instant S1 signal. During the latter step, ionised electrons can escape and generate an S2 signal by exciting atoms under the influence of a strong field. The background particles interact with atomic electrons thus producing a different signal ratio $\left(\frac{S1}{S2}\right)$, which can be used to distinguish WIMP interactions. The scintillation signals are detected by photodetectors such as PMTs (XENON1T [60], XENON-100 [61], LUX [62], PandaX [63]), PDMs[1] (DarkSide-50 [24]), NUV-HD SiPMs[2] (DarkSide-20k [64]) .

[1] Assembled SiPMs referred to as photodetector modules
[2] Near Ultraviolet High Density SiPMs manufactured by FBK

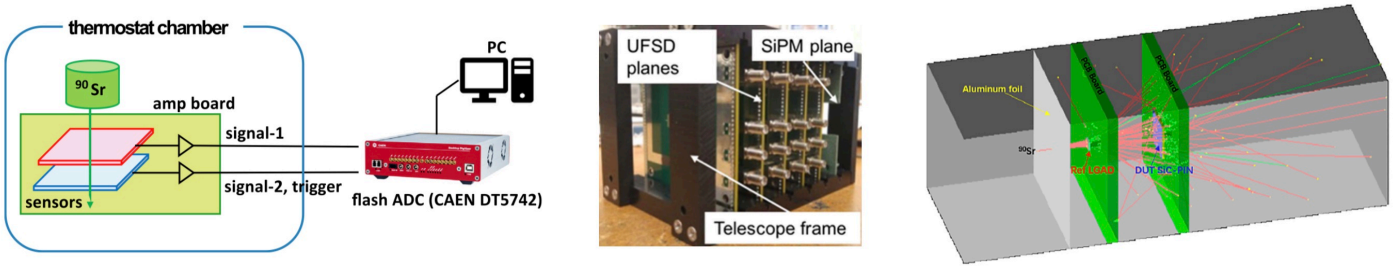

(a) (b) (c)

Figure 21: Experimental setups for measuring the time resolution of detectors. Setup (a) used a ^{90}Sr β source. The two sensors, placed at a thermostat chamber, were triggered by β sources and the signals were fed to the ADC [41]. Setup (b) aligned four UFSDs and a SiPM [14]. Setup (c) was intended to study the time resolution of SiC-PIN detectors and used LGAD as reference [42].

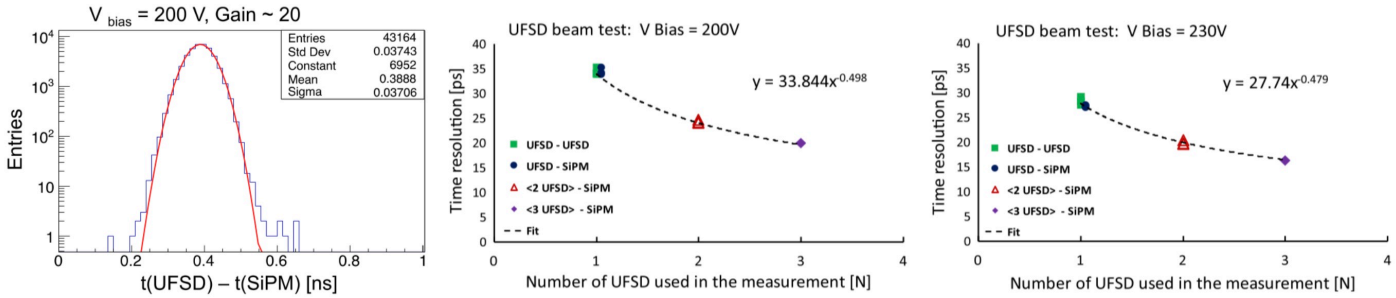

(a) (b) (c)

Figure 22: Test results from Figure 21 (b). Figure (a) shows the Gaussian fit of the time difference of UFSD and SiPM with a time resolution of 37 ps. Figure (b), (c) show the time resolution calculated from the difference and from the average of detectors.

Table 2: Applications for semiconductor detectors. The applications of high energy physics are coloured blue, while the medical applications are coloured red. If the type includes APD, it is compatible with all types of avalanche diodes, with a preference for the second specific type.

Type	Applications	Advantages	Ref.
PMT	Super-Kamiokande	Low DCR	[43, 44] (1996)[a]
SiPM	Time-domain functional Near-infrared Spectroscopy (TD fNIRS)	Compact, EM immunity	[45] (2016)
SiPM	Measurement of higher order photon correlations using PNRD[b]	Large dynamic range of count rates	[46] (2017)
SiPM	Dark matter detection (eg: DarkSide-50 LAr TPC[c] using PDM[d])	Better performance at LAr temp.	[24] (2018)
SiPM-Scintillator	γ–ray detection in borehole logging. (Typical source: ^{40}K, ^{241}Am)	Compact, low-voltage	[47] (2021)
SiPM-LYSO[e]	X-ray communication (XCOM) during spacecraft reentry blackout.	X-ray pass the plasma sheath without attenuation	[48] (2021)
SiPM-LYSO	The CMS MTD detector designed to measure the MIPs with σ_t = 20 ps	Radiation tolerance of LYSO	[49] (2020)
SiPM-LYSO/LFS-3	Positron Annihilation Lifetime Spectroscopy (PALS)[f]	Compact, high quantum efficiency	[50] (2020)
APD/SiPM	Time-of-flight Positron Emission Tomography (TOF-PET)	EM immunity	[51] (2021)
UFSD (LGAD)	ATLAS HGTD for HL-LHC, CT-PPS	Time resolution	[52, 29] (2018)
APD/SiPM	Photodetectors for light detection and ranging (LIDAR)		[53] (2020)
APD/NFAD[g]	Quantum Random Number Generation (QRNG)	Low noise	[54] (2020)

[a] The experiment started in 1996.
[b] PNRD: Photon Number Resolving Detectors.
[c] Liquid Argon Time Projection Chamber (LAr TPC)
[d] Arrays of SiPMs arranged in assemblies called photodetector modules (PDMs).
[e] Lutetium–yttrium oxyorthosilicate (LYSO) scintillator coupled with SiPM
[f] The positron will reside in the voids of solids and emit γ–rays at a slower rate, enabling the detection of defects and voids.
[g] NFAD (SPAD): Negative Feedback InGaAs/InP Single Photon Avalanche Diode, with faster quenching and suppression of the afterpulse [55, 56].

8 Conclusion and outlook

This article introduced the fundamental operating principles of particle detection. Theoretical and practical measurements regarding the sources of time uncertainty are provided. The detectors based on avalanches have a wide range of applications. The exploration of SiPM is a popular and rapidly developing field, with new products being introduced nearly every year, posing challenges for the front-end readout electronics. In terms of radiation damage, power consumption, and detector size, the detectors intended for academic research face challenges. The UFSD developed during these years has the capacity to address these issues. In addition to being a novel type of semiconductor detector, the AC-LGAD makes use of charge sharing to improve time performance and drastically reduce the required number of channels.

References

[1] Cristián H. Peña and on behalf of the CMS Collaboration. Precision timing with the cms mip timing detector. Journal of Physics: Conference Series, 2019. 10.1088/1742-6596/1162/1/012035.

[2] Ivor Fleck, Maxim Titov. Handbook of Particle Detection and Imaging. Springer, 2 edition, 2021.

[3] Passsage of particles through matter, https://pdg.lbl.gov/2019/reviews/rpp2018-rev-passage-particles-matter.pdf.

[4] Sirunyan A.M. et al. Performance of the CMS muon detector and muon reconstruction with proton-proton collisions at $\sqrt{s}$ = 13 TeV. JINST, 2018. 10.1088/1748-0221/13/06/P06015.

[5] Laura Zani. The silicon vertex detector of the belle ii experiment. Nuclear Instruments and Methods in Physics Research Section A: Accelerators, Spectrometers, Detectors and Associated Equipment, 2022. 10.1016/j.nima.2022.166952.

[6] F Nessi-Tedaldi. Overview of pbwo4 calorimeter in cms. Nuclear Instruments and Methods in Physics Research Section A: Accelerators, Spectrometers, Detectors and Associated Equipment, 1998. 10.1016/S0168-9002(98)00321-0.

[7] P. Strizenec. Performance of the atlas liquid argon calorimeter after three years of lhc operation and plans for a future upgrade. Journal of Instrumentation, September 2014. 10.1088/1748-0221/9/09/C09007.

[8] R. J. Cooper, M. Amman, and K. Vetter. High resolution gamma-ray spectroscopy at high count rates with a prototype high purity germanium detector. Nuclear Instruments and Methods in Physics Research Section A: Accelerators, Spectrometers, Detectors and Associated Equipment, 2018. 10.1016/j.nima.2017.12.053.

[9] Lato ová el al. Characterization of the polysilicon resistor in silicon strip sensors for atlas inner tracker as a function of temperature, pre- and post-irradiation.

[10] V. Manzari. Silicon detectors, https://indico.cern.ch/event/453690/sessions/99350/attachments/1184199/1726998/2015-11_SiliconDetectors_manzari_Lecture2.pdf.

[11] Heinrich Schindler. Microscopic Simulation of Particle Detectors, 2012. https://cds.cern.ch/record/1500583.

[12] Hartmut F-W Sadrozinski, Abraham Seiden, and Nicolò Cartiglia. 4d tracking with ultra-fast silicon detectors. Reports on Progress in Physics, dec 2017. 10.1088/1361-6633/aa94d3.

[13] W. Riegler and G. Aglieri Rinella. Time resolution of silicon pixel sensors. Journal of Instrumentation, nov 2017. 10.1088/1748-0221/12/11/P11017.

[14] N. Cartiglia et al. Beam test results of a 16ps timing system based on ultra-fast silicon detectors. Nuclear Instruments and Methods in Physics Research Section A: Accelerators, Spectrometers, Detectors and Associated Equipment, 2017. ISSN 0168-9002. 10.1016/j.nima.2017.01.021.

[15] Cartiglia et al. Performance of ultra-fast silicon detectors. Journal of Instrumentation, 2014. 10.1088/1748-0221/9/02/C02001.

[16] Tsigaridas S. et al. Timewalk correction for the timepix3 chip obtained with real particle data. Nuclear Instruments and Methods in Physics Research Section A: Accelerators, Spectrometers, Detectors and Associated Equipment, 2019. 10.1016/j.nima.2019.03.077.

[17] Canali C. et al. Drift velocity of electrons and holes and associated anisotropic effects in silicon. Journal of Physics and Chemistry of Solids, 1971. 10.1016/S0022-3697(71)80137-3.

[18] P. Webb and A. R. Jones. Large area reach-through avalanche diodes for radiation monitoring. IEEE Transactions on Nuclear Science, 1974. 10.1109/TNS.1974.4327455.

[19] W. Riegler and P. Windischhofer. Time resolution and efficiency of spads and sipms for photons and charged particles. Nuclear Instruments and Methods in Physics Research Section A: Accelerators, Spectrometers, Detectors and Associated Equipment, 2021. 10.1016/j.nima.2021.165265.

[20] Acerbi Fabio et al. Cryogenic characterization of fbk hd near-uv sensitive sipms. IEEE Transactions on Electron Devices, 2017. 10.1109/TED.2016.2641586.

[21] Degenhardt Carsten et al. The digital silicon photomultiplier — a novel sensor for the detection of scintillation light. In 2009 IEEE Nuclear Science Symposium Conference Record (NSS/MIC), 2009. 10.1109/NSSMIC.2009.5402190.

[22] Frach Thomas et al. The digital silicon photomultiplier — principle of operation and intrinsic detector performance. In 2009 IEEE Nuclear Science Symposium Conference Record (NSS/MIC), 2009. 10.1109/NSSMIC.2009.5402143.

[23] Gersbach M. et al. A parallel 32×32 time-to-digital converter array fabricated in a 130 nm imaging cmos technology. In 2009 Proceedings of ESSCIRC, September 2009. 10.1109/ESSCIRC.2009.5326021.

[24] Aalseth C. E. et al. Darkside-20k: A 20 tonne two-phase lar tpc for direct dark matter detection at lngs. The European Physical Journal Plus, 2018. 10.1140/epjp/i2018-11973-4.

[25] Andreas Beling and Joe C. Campbell. Chapter 3 - advances in photodetectors and optical receivers. In Optical Fiber Telecommunications (Sixth Edition), Optics and Photonics. Academic Press, Boston, 2013. 10.1016/B978-0-12-396958-3.00003-2.

[26] Moffat N. et al. Low gain avalanche detectors (lgad) for particle physics and synchrotron applications. Journal of Instrumentation, 2018. 10.1088/1748-0221/13/03/C03014.

[27] RD50 collaboration.

[28] HL-LHC, 10.5170/CERN-2015-005.

[29] Fabio Ravera. The CT-PPS project: detector hardware and operational experience. 10.22323/1.309.0015.

[30] I. Smirnov. HEED, program to compute energy loss of fast particles in gases, version 1.01, Cern.

[31] Ware et al. Calibrating photon-counting detectors to high accuracy: background and deadtime issues. Journal of Modern Optics, 2007. 10.1080/09500340600759597.

[32] Y. et al. Kang. Dark count probability and quantum efficiency of avalanche photodiodes for single-photon detection. Applied Physics Letters, 2003. 10.1063/1.1616666.

[33] S. M. Sze. Physics of Semiconductor Devices. 1981.

[34] Acerbi et al. Characterization of single-photon time resolution: From single spad to silicon photomultiplier. IEEE Transactions on Nuclear Science, 2014. 10.1109/TNS.2014.2347131.

[35] Piemonte et al. Characterization of the first fbk high-density cell silicon photomultiplier technology. IEEE Transactions on Electron Devices, 2013. 10.1109/TED.2013.2266797.

[36] Hamamatsu sipm product datasheet, https://www.hamamatsu.com/eu/en/product/optical-sensors/mppc/mppc_mppc-array.html, .

[37] T. Nagano, K. Sato, A. Ishida, T. Baba, R. Tsuchiya, and K. Yamamoto. Timing resolution improvement of mppc for tof-pet imaging. In 2012 IEEE Nuclear Science Symposium and Medical Imaging Conference Record (NSS/MIC), 2012. 10.1109/NSSMIC.2012.6551376.

[38] Sadrozinski et al. Ultra-fast silicon detectors (ufsd). Nuclear Instruments and Methods in Physics Research Section A: Accelerators, Spectrometers, Detectors and Associated Equipment, 2016. 10.1016/j.nima.2016.03.093.

[39] N. et al. Cartiglia. Design optimization of ultra-fast silicon detectors. Nuclear Instruments and Methods in Physics Research Section A: Accelerators, Spectrometers, Detectors and Associated Equipment, 2015. 10.1016/j.nima.2015.04.025.

[40] Xin Yu, Haojie Xia, Weishi Li, Jin Zhang, and Songtao Chang. A 4.8 ps root-mean-square resolution time-to-digital converter implemented in a 20 nm cyclone-10 gx field-programmable gate array. Review of Scientific Instruments, 2022. 10.1063/5.0090783.

[41] Kyoji Onaru, Kazuhiko Hara, Daigo Harada, Sayaka Wada, Koji Nakamura, and Yoshinobu Unno. Study of time resolution of low-gain avalanche detectors. Nuclear Instruments and Methods in Physics Research Section A: Accelerators, Spectrometers, Detectors and Associated Equipment, 2021. 10.1016/j.nima.2020.164664.

[42] Yang et al. Time resolution of the 4h-sic pin detector. Frontiers in Physics, 2022. 10.3389/fphy.2022.718071.

[43] Super-Kamiokande, https://www-sk.icrr.u-tokyo.ac.jp/sk/, .

[44] Super-Kamiokande U.S. Home Page, https://web.archive.org/web/20040130175750/http://www.phys.washington.edu/~superk/, .

[45] Rebecca et al. Probe-hosted silicon photomultipliers for time-domain functional near-infrared spectroscopy: phantom and in vivo tests. Neurophotonics, 2016. 10.1117/1.NPh.3.4.045004.

[46] Gasparini Leonardo et al. Sipm in g(2) measurements. In Quantum Information and Measurement (QIM) 2017 (2017), paper QT6A.46. Optica Publishing Group, 2017. 10.1364/QIM.2017.QT6A.46.

[47] A. et al. Bala. Operation of scintillators and sipms at high temperatures and their application for borehole logging. Nuclear Instruments and Methods in Physics Research Section A: Accelerators, Spectrometers, Detectors and Associated Equipment, 2021. 10.1016/j.nima.2021.165161.

[48] Yunpeng Liu, Peng Dang, Xiaobin Tang, Junxu Mu, and Zhaopeng Feng. Performance analysis of lyso–sipm detection module for x-ray communication during spacecraft reentry blackout. Nuclear Instruments and Methods in Physics Research Section A: Accelerators, Spectrometers, Detectors and Associated Equipment, 2021. 10.1016/j.nima.2021.165673.

[49] M. Malberti. Precision timing with lyso:ce crystals and sipm sensors in the cms mtd barrel timing layer. Journal of Instrumentation, 2020. 10.1088/1748-0221/15/04/C04014.

[50] Wang et al. A new sipm-based positron annihilation lifetime spectrometer using lyso and lfs-3 scintillators. Nuclear Instruments and Methods in Physics Research Section A: Accelerators, Spectrometers, Detectors and Associated Equipment, 2020. 10.1016/j.nima.2020.163662.

[51] P. Lecoq and S. Gundacker. SiPM applications in positron emission tomography: toward ultimate PET time-of-flight resolution. The European Physical Journal Plus, 2021. 10.1140/epjp/s13360-021-01183-8.

[52] Corentin Allaire. A High-Granularity Timing Detector (HGTD) in ATLAS : Performance at the HL-LHC. Technical report, CERN, Geneva, 2018.

[53] Hamamatsu photodetectors for lidar, https://www.hamamatsu.com/content/dam/hamamatsu-photonics/sites/documents/99_SALES_LIBRARY/ssd/Photodetector_lidar_kapd0005e.pdf, .

[54] Leone et al. An optical chip for self-testing quantum random number generation. APL Photonics, October 2020. 10.1063/5.0022526.

[55] Free-Running Single Photon Detectors in the Near-Infrared Band manufacturered by QuantumCTek, http://www.quantum-info.com/English/product/pfour/danguangzitanceqi/2021/0901/672.html, .

[56] Quantum Random Number Generator manufacturered by QuantumCTek, http://www.quantum-comm.com/English/product/coredevice/2017/0831/301.html, .

[57] Stefan Gundacker and Arjan Heering. The silicon photomultiplier: fundamentals and applications of a modern solid-state photon detector. Physics in Medicine & Biology, 2020. 10.1088/1361-6560/ab7b2d.

[58] Dalla Mora et al. The sipm revolution in time-domain diffuse optics. Nuclear Instruments and Methods in Physics Research Section A: Accelerators, Spectrometers, Detectors and Associated Equipment, 2020. 10.1016/j.nima.2020.164411.

[59] A. Von Chong, M. Terosiet, A. Histace, and O. Romain. Pulse oximetry using a buried quad junction photodetector. In 2016 IEEE International Conference on Electronics, Circuits and Systems (ICECS), 2016. 10.1109/ICECS.2016.7841223.

[60] Xenon1t homepage, http://www.xenon1t.org/, .

[61] Xenon-100 homepage, http://xenon.astro.columbia.edu/XENON100_Experiment/, .

[62] Akerib D. S. et al. Investigation of background electron emission in the lux detector. Phys. Rev. D, 2020. 10.1103/PhysRevD.102.092004.

[63] PandaX-II Collaboration. Dark matter search results from the commissioning run of pandax-ii. Physical Review D, 2016. 10.1103/PhysRevD.93.122009.

[64] Aalseth C. E. et al. Darkside-20k: A 20 tonne two-phase lar tpc for direct dark matter detection at lngs. The European Physical Journal Plus, 2018. 10.1140/epjp/i2018-11973-4.